

Non-Aqueous One-Pot SnO₂ Nanoparticle Inks and Their Use in Printable Perovskite Solar Cells

T. A. Nirmal Peiris, Hasitha C. Weerasinghe, Manoj Sharma, Jueng-Eun Kim, Monika Michalska, Naresh Chandrasekaran, Dimuthu C. Senevirathna, Hanchen Li, Anthony S. R. Chesman, Doojin Vak, and Jacek J. Jasieniak*



Cite This: *Chem. Mater.* 2022, 34, 5535–5545



Read Online

ACCESS |

Metrics & More

Article Recommendations

Supporting Information

ABSTRACT: Metal halide perovskite materials are promising candidates for printable solar cells due to their feasibility for achieving high device efficiency at a low processing temperature. One of the key challenges in printed perovskite solar cell (PSC) research is to develop low-temperature-processable charge-transporting layers for both electron and hole-transporting materials, which can be used within large-scale roll-to-roll (R2R) printing techniques. Colloidal links allow for facile deposition, provided that the size of the nanoparticles (NPs) is controlled to less than a few tens of nanometres (ideally < 20 nm); they can be deposited as uniform films and can be processed at low temperatures (typically < 140 °C). Here, we report a facile and scalable route for the synthesis of SnO₂ NP dispersions using a microwave-assisted “benzyl alcohol” approach that is compatible with all of these R2R printing requirements. The method enables crystalline SnO₂ NPs to be synthesized with a controlled average particle size (~6.5 nm) and be used directly as an ink without any post-synthesis purification (i.e., one-pot synthesis). The use of these SnO₂ NPs has been explored as an electron transport layer (ETL) within planar PSCs using spin-coating and thermal processing at 140 °C for 2 min, yielding devices with over 18% photo-conversion efficiency. Comparable devices were also fabricated using slot die-coated SnO₂ on glass substrates and R2R-coated SnO₂ on plastic substrates, yielding efficiencies of 15.3 and 10.4%, respectively. Our results demonstrate the suitability of the developed SnO₂ ink to be used for the deposition of ETLs in optoelectronic devices by industrial-scale R2R printing processes.



INTRODUCTION

The soaring increase in the device performance of organic-inorganic halide perovskite solar cells (PSCs) has led the photovoltaic (PV) research community to now focus on the challenges associated with their commercialization.¹ Among these challenges is the need to scale the fabrication process. Large-scale roll-to-roll (R2R) printing is considered a promising industrial approach for the production of large-area flexible PSC modules due to its higher throughput, energy efficiency, and low environmental impact.² Thus far, the highest-reported PSC efficiencies (>25%) have been achieved for small-scale devices with an active device area of <1 cm² and were fabricated using methods that do not lend themselves to large-area fabrication processes.^{3,4} Translation of these advances into R2R-printed PSCs has been rather sluggish, arising largely because of the challenges in large-scale printing, which are compounded by the fact that ink formulations are not typically compatible between spin-coating and R2R coating.^{5,6} Therefore, an ongoing need exists to develop tailored inks for the perovskite absorber, the charge-transporting layer, and the top electrode that are conducive toward large-scale printing. In this work, we focus on the development of SnO₂ inks that are suitable for use as electron transport

layers in PSCs and are compatible with both small-scale and R2R deposition.

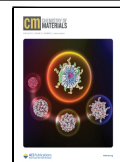
In the R2R printing of solar cells, plastic substrates (typically polyethylene terephthalate, PET) are desirable for their transparency, flexibility, and toughness but are often susceptible to degradation and dimensional distortion at a high temperature (>140 °C).⁷ Due to this temperature limitation, additional research efforts are required to develop low-temperature-processable charge-transporting material inks that can be used in fabricating efficient charge-transporting layers by R2R printing in order to commercialize this PV technology.

Many of the solution-processable charge-transporting materials currently used in PSCs are organic-based. While enabling low-temperature processability, they also often result in diminished solar cell performance with time due to their instability in air and moisture.⁸ Replacing these with inorganic

Received: February 23, 2022

Revised: May 9, 2022

Published: June 16, 2022



metal oxides in PSCs has the prospect to improve the long-term stability of the devices and given that most organic materials are costly, they also reduce the production cost.^{9–11} However, unlike organic-based materials, typical inorganic-based charge-transporting materials require higher temperature annealing to induce enhanced inter-particle and particle–substrate interactions to achieve appropriate structural and charge-transporting properties.¹²

TiO_2 is the most widely used inorganic electron-transporting material in n-i-p PSCs. It usually requires a high sintering temperature of $>450\text{ }^\circ\text{C}$ for efficient electron transport, which is an obstacle to its integration into flexible devices using R2R printing on plastic substrates.¹³ Recently, SnO_2 has emerged as an effective electron transporting layer (ETL) in PSCs owing to its wider band gap and higher mobility compared with TiO_2 .¹⁴ In addition, the low-temperature processing capabilities of SnO_2 have made it a good candidate to be used with R2R printing conditions to fabricate ETLs for n-i-p PSCs.¹⁵ In most cases, SnO_2 ETLs in PSCs have been prepared by spin-coating a $\text{SnCl}_4 \cdot 5\text{H}_2\text{O}$ or $\text{SnCl}_2 \cdot 2\text{H}_2\text{O}$ precursor solution on conducting substrates.^{16,17} As these methods require annealing at $>150\text{ }^\circ\text{C}$ for efficient conversion of $\text{Sn}^{2+}/\text{Sn}^{4+}$ into SnO_2 , this approach is not suitable for the fabrication of SnO_2 layers on flexible PET substrates using R2R processes. Similarly, the use of pre-synthesized water-based SnO_2 inks to fabricate SnO_2 ETLs within n-i-p structured PSCs also requires annealing at $>150\text{ }^\circ\text{C}$ to remove any residual water in the ETL. This may lead to perovskite degradation, thereby decreasing the device efficiency and long-term stability.^{18,19} Moreover, fabricating uniform films using such commercially available water-based inks is extremely challenging due to their poor wetting properties with indium tin oxide (ITO)/plastic substrates.²⁰ These factors indicate that further synthetic efforts are required to develop truly low-temperature processable, high-quality, and effective SnO_2 charge-transport layers for high-efficiency PSCs. Appropriately engineered SnO_2 nanoparticle (NP) inks are well placed to achieve these requirements.

Several different methods have been investigated as routes for the synthesis of SnO_2 NPs with different size ranges and distributions, which include spray pyrolysis,²¹ hydrothermal methods,²² thermal evaporation,²³ gel combustion,²⁴ sol–gel method,²⁵ and electrochemical synthesis.²⁶ Most of these processes usually require the use of high temperatures, high pressures, high boiling points, or mixed solvents, and expensive organic tin precursors that are often toxic and require a complicated synthesis procedures, involving multiple processing steps. For instance, Wong et al. developed a high-pressure solvothermal system to adjust the shape of SnO_2 crystals and build the 3D configuration at the later stage of crystal growth. In that work, 3D-ordered SnO_2 particles were achieved by heating the reaction mixture at $220\text{ }^\circ\text{C}$ with an applied pressure of 200 MPa for 24 h.²⁷ Similarly, SnO_2 NPs with a size of ca. 14 nm were synthesized using a precipitation route followed by a hydrothermal treatment in an ammonia solution for 3 h under a pressure and temperature of 10 MPa and $200\text{ }^\circ\text{C}$, respectively.²⁸ Wang et al. used a solvothermal route to synthesize SnO_2 NPs with a size of ca. 2.5 nm. The synthesis was carried out in an autoclave at $180\text{ }^\circ\text{C}$ by transferring the reaction mixture containing the Sn precursor in a mixed solvent of oleic acid, oleylamine, and ethanol. In that synthesis, toxic solvents such as cyclohexane and chloroform were used in washing and final dispersion steps.²⁹ A solution approach

was employed by Xin et al. by heating SnCl_2 in ethylene glycol via a reflux process at $190\text{ }^\circ\text{C}$.³⁰ Likewise, Fujihara et al. performed hydrolysis of SnCl_4 in deionized water under refluxing conditions to yield SnO_2 precipitates, followed by a hydrothermal treatment to produce SnO_2 NPs with an average particle size of $\sim 4\text{ nm}$.³¹

In recent years, microwaves have started to be explored as an efficient alternative energy source to traditional forms of heating in material synthesis and processing.^{32–34} It has been demonstrated that using microwaves for the SnO_2 NP synthesis could reduce the reaction time over conventional non-aqueous sol–gel synthesis and allow for a more precise control of the reaction parameters, all in favor of a higher yield and reproducibility.³⁵ Srivastava et al. used a microwave-induced heating method to obtain SnO_2 NPs with an average size of $\sim 10\text{ nm}$.³⁶ A similar microwave-assisted synthesis route was employed to synthesize narrowly distributed SnO_2 NPs with an average particle size of $\sim 10\text{ nm}$ without possessing any post-synthesis modifications.³⁷ Yoshida et al. reported a microwave-assisted hydrothermal synthesis route to achieve size-controlled SnO_2 NPs (average size from ~ 11 to 26 nm) by varying the SnCl_4 concentration in an ethanol–water solvent mixture.³⁸ However, most of the reported methods to produce SnO_2 NP dispersions are not scalable. Therefore, there is a need to either change or modify these existing methodologies or design novel synthetic routes for the scalable production of SnO_2 NP inks that are suitable for large-scale printed PV applications.

In this study, we address these challenges by developing a simple and scalable one-pot microwave-assisted synthesis to obtain SnO_2 nanocrystal inks that can be used in fabricating low-temperature-processable SnO_2 ETLs in PSCs by R2R printing techniques. Microwave-assisted heating for inorganic material synthesis is known to be advantageous compared to traditional radiant heating due to its efficient and homogenous heat generation throughout the reaction mixture within a few seconds.^{39,40} However, these reaction conditions can only be achieved through the use of a suitable microwave-absorbing solvent system. Here, we have selectively used an ethanol and benzyl alcohol mixture to fulfill this function, with the latter also acting as a suitable ligand for the SnO_2 NPs.⁴¹ Through optimization of the reaction temperature, time, and solvent mixture, suitable SnO_2 NP dispersions are achieved that can be used directly to fabricate SnO_2 thin films by spin-coating, slot-die coating, or R2R printing (see Figure 1). Importantly, the

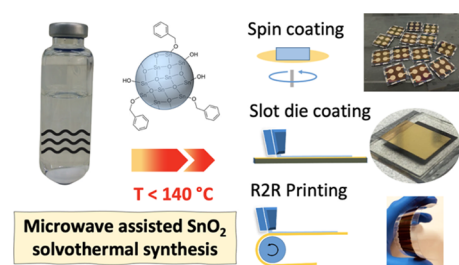


Figure 1. Schematic representation of benzyl alkoxide-stabilized SnO_2 NPs obtained from a simple one-pot synthesis. These dispersions allow for the fabrication of thin films directly from the reaction mixture (or by diluting appropriately) on glass or plastic substrates at a low temperature ($140\text{ }^\circ\text{C}$). Such thin films are suitable for use as electron transport layers within PSCs fabricated using spin coating, slot-die coating, and large-scale R2R printing techniques.

one-pot nature of the developed synthesis removes any need for purification, which minimizes chemical waste, saves time, and can dramatically enhance reproducibility at the laboratory and industrial scales.⁴² Furthermore, these developed SnO₂ NP inks can be processed at temperatures of 140 °C and below, which renders them suitable for use as ETLs in PSCs on both glass and plastic substrates.

■ EXPERIMENTAL SECTION

Materials. All materials were used as purchased without further purification. Tin(IV) chloride pentahydrate (SnCl₄·5H₂O), anhydrous benzyl alcohol, anhydrous ethanol, 2-propanol (IPA), acetone, N,N-dimethylformamide (DMF), dimethyl sulfoxide (DMSO), 4-*tert*-butylpyridine (TBP), bis(trifluoromethane)sulfonimide lithium salt (Li-TFSI), cesium iodide (CsI), anhydrous acetonitrile, and anhydrous chlorobenzene were purchased from Sigma-Aldrich. Tin(IV) oxide (15 wt % in H₂O colloidal dispersion), lead iodide (PbI₂), and lead bromide (PbBr₂) were purchased from Alfa Aesar. Spiro-OMeTAD was purchased from Lumtec. Formamidinium iodide (FAI), methylammonium bromide (MABr), and FK 209 Co-TFSI salt were purchased from GreatCell.

SnO₂ NP Synthesis. For a typical SnO₂ NP synthesis, the reaction precursor was prepared by dissolving 0.65 g of SnCl₄·5H₂O in a 20 mL mixture of benzyl alcohol and absolute ethanol (50 by vol %) in air. After the complete dissolution of the salt, the precursor solution was filtered using a 0.45 μm pore size Minisart filter before being transferred into the microwave reaction vial. Then, the vial was sealed with a headspace cap in air and transferred to a microwave reactor cavity (Biotage Initiator Classic, with a maximum power of 400 W). The reaction was carried out at the desired temperature for 30 min under continuous microwave irradiation. The resulting clear solution with SnO₂ NPs was diluted with IPA and used without any purification.

PSC Fabrication and Characterization. The n-i-p structured PSCs were fabricated on a pre-patterned fluorine-doped tin oxide (FTO)-coated glass (Latech, 15 Ω/sq) or a custom-patterned flexible tin doped indium oxide (ITO) (8 Ω sq⁻¹, the OPV8 substrate manufactured by Solutia and patterned by Meko Print). FTO substrates were sonicated for 10 min each in successive baths of Hellmanex detergent, acetone, and IPA. Then, the samples were dried under a nitrogen stream before being exposed to air–oxygen plasma (Harrick Plasma) at an RF power of 18 W for 15 min. For devices fabricated using spin-coating, the SnO₂ ETL was spin-coated using 5 mL of the SnO₂ ink diluted with IPA (SnO₂ reaction mixture/IPA—2:3 by vol % + 25 μL from 6 mg/1 mL PEG 400 in IPA) at 4000 rpm for 20 s on cleaned FTO glass substrates, and the layer was annealed at 140 °C for 2 min on a pre-heated hot plate. The slot-die coating was carried out on a pre-heated FTO glass substrate at 80 °C using the same ink with a coating speed of 15 mm/s and a 4 mm wide meniscus guide. After coating, the substrates were left for another 2 min for further drying at the same temperature. The spin and slot-die coating of SnO₂ was performed under ambient conditions in a fume hood cabinet with an average temperature and relative humidity (RH) of 22 °C and 50%, respectively.

An ITO-coated PET roll was used as the substrate to deposit SnO₂ ETLs a R2R process, and the substrate was not cleaned before coating. The deposition of the SnO₂ ETL on the plastic substrate was conducted using a slot-die setup connected to a commercial R2R coater (Mini-Labo, Yasui Seki). The coating speed was controlled using a built-in controller of the R2R coater, while the solution flow through the slot-die head was controlled using a syringe pump. The SnO₂ layer was printed on the plastic substrate at a constant roller speed of 0.3 m/min and a flow rate of 30 μL/min (using a 13 mm wide meniscus guide), and the film was dried under a 120 °C blow heater before moving over a 135 °C curved hot plate for 12 s. This coating process was conducted in air with an average temperature and RH of 24 °C and 60%, respectively. A short video clip is attached in the Supporting Information demonstrating the slot-die coating of SnO₂ on ITO flexible substrates within a R2R process. A section of

R2R-coated SnO₂ electrodes was cut into smaller 2 cm² pieces and then mounted onto glass substrates for the deposition of the perovskite and spiro-OMeTAD layers by spin-coating.

The perovskite precursor solution was prepared by dissolving FAI (190.03 mg, 1.105 mmol), PbI₂ (548.60 mg, 1.19 mmol), MABr (21.83 mg, 0.195 mmol), PbBr₂ (77.07 mg, 0.21 mmol), and CsI (15.59 mg, 0.062 mmol) in 800 μL of the DMF/DMSO (8:2) co-solvent. 20 μL of KI was added to the perovskite precursor from a stock solution made by dissolving 332 mg of KI in 1 mL of DMSO. This acted as a dopant to reduce hysteresis as reported.¹⁹ The perovskite precursor solution was coated onto the SnO₂ ETL in a sequential two-step spin-coating process at 1000 and 6000 rpm for 10 and 20 s, respectively. Just 5 s before finishing the second spin-coating step, the substrates were treated with drop-cast chlorobenzene (~350 μL) and then annealed at 100 °C for 1 h. The spiro-OMeTAD solution was prepared by dissolving 73 mg of spiro-MeOTAD in 1 mL of chlorobenzene in addition to 30 μL of TBP, 18 μL from the Li-TFSI stock solution (520 mg of Li-TFSI in 1 mL of acetonitrile), and 29 μL from the FK 209 Co(III) TFSI salt stock solution (67.6 mg of FK 209 Co(III) TFSI salt in 200 μL of acetonitrile). The spiro-OMeTAD was spin-coated onto the perovskite layer at 3000 rpm for 30 s. Finally, an 80 nm thick layer of gold was thermally evaporated under a baseline pressure of less than 8 × 10⁻⁶ Torr (thermal evaporator systems, DD-GCM03CT). The masked active area of the devices was 0.16 cm².

Particle size distributions were measured with a particle size analyzer (Malvern Zetasizer Nano-ZS). The water contact angle of the SnO₂ films was monitored using a contact angle system from OCA. The transmission electron microscopy (TEM) images of SnO₂ NPs were measured using the FEI Tecnai G2 T20 TWIN transmission electron microscope. Scanning electron microscopy (SEM) images were taken at 5 V accelerating voltage and a beam aperture of 30 μm using a FEI Magellan 400 FEG-SEM. Thermogravimetric analysis (TGA) was conducted using a Mettler Toledo TGA2. The Fourier-transform infrared spectroscopy (FT-IR) spectra were collected using an FT-IR spectrophotometer (Nicolet 6700), and UV-vis absorption was obtained by performing the transmission and reflection measurements of the films coated on quartz substrates using an integrating sphere connected to a PerkinElmer Lambda 950 spectrometer. The structure of the films was investigated by X-ray diffraction (XRD) on Bruker D8 Discover with a Cu Kα radiation source ($\lambda = 1.5418 \text{ \AA}$). The elemental composition and Fermi level (WF) of the SnO₂ on FTO glass were derived from X-ray photoelectron spectroscopy (Nexsa, Thermo Fisher Scientific). Al Kα and He(I) sources (21.21 eV) with a pass energy of 200 eV (50 eV for a narrow scan) and 3 eV were used to emit X-ray and UV photons, respectively. The measurement was conducted with a chamber pressure below 5.0 × 10⁻⁸ Torr. The XPS narrow scan line profile was decomposed into peaks fitted using Gaussian (70%) and Lorentzian (30%). The Shirley function was used for background correction.⁴³ The valence-band-level of these systems was calculated using the standard relation: VB = 21.21 (hv) − (E_{cutoff} − E_{VB}). Photoluminescence (PL) emission measurements were conducted using a Cary Eclipse fluorescence spectrometer (Agilent Technologies). Atomic force microscopy (AFM) and conductive AFM images of SnO₂-coated films on ITO glass substrates were obtained using Bruker Dimension Icon AFM. AFM images were taken in the PeakForce Tapping mode using TESPA-V2 probes (tip radius-of-curvature = ~7 nm, resonant frequency (f_0) = 320 kHz, spring constant (k) = 37 N/m). J-V measurements of solar cells were performed with a BioLogic potentiostat/galvanostat VMP3 and an ABET Technology Sun 3000 class AAA solar simulator calibrated to AM 1.5G sun. The incident photon-to-electron conversion efficiency (IPCE) measurements were performed at zero bias by illuminating the device with monochromatic light supplied from a tungsten lamp (Newport 250 W QTH) in combination with a Newport Oriel cornerstone 260 monochromator. The number of incident photons on the samples was measured using a Keithley 2000 m for each wavelength, and a Si photodiode (Thorlabs SM05SPD2A) was used for the calibration.

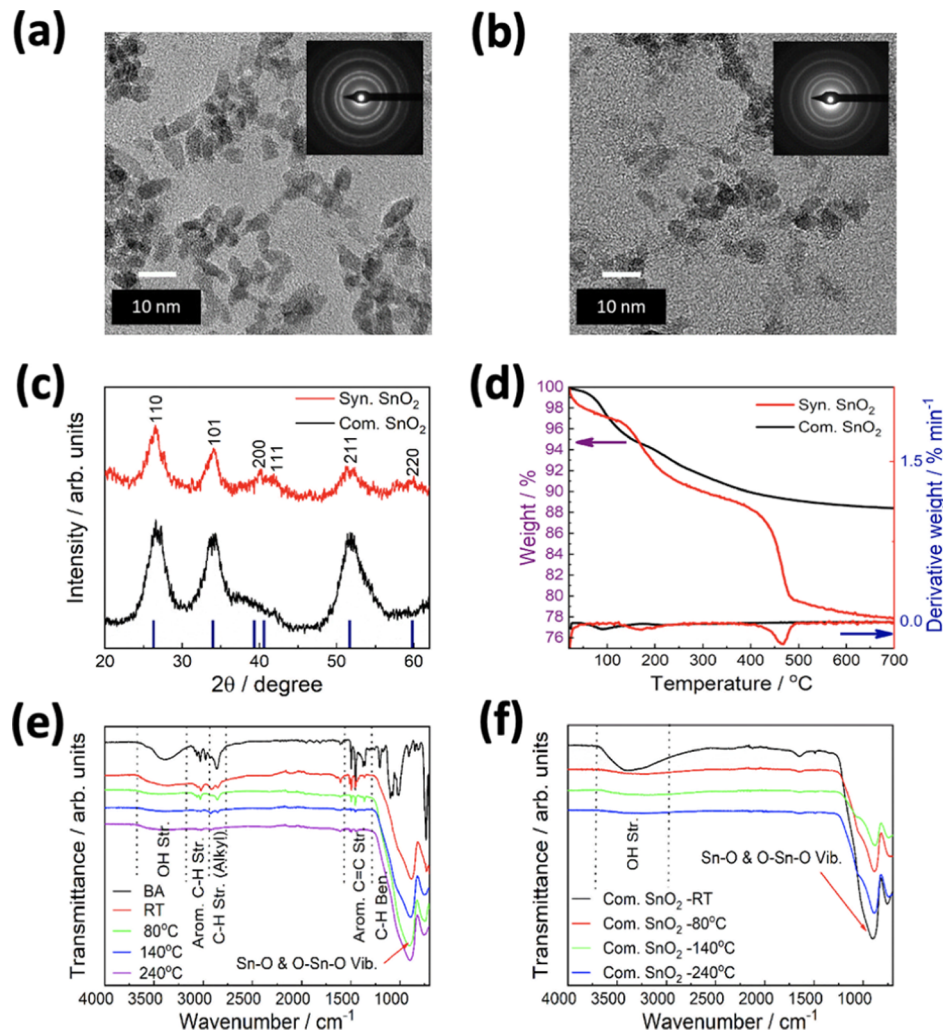


Figure 2. TEM images of (a) synthesized SnO₂ NPs and (b) commercial SnO₂ NPs, with the SAED patterns included in the insets. (c) XRD patterns of synthesized and commercial SnO₂ NPs, as well as indexed diffraction peaks included in JCPDS card no. 41-1445. (d) Thermogravimetric plots of synthesized and commercial SnO₂ NPs. FTIR spectra of (e) benzyl alcohol and synthesized SnO₂ NPs and (f) commercial SnO₂ NPs annealed at different temperatures for 2 min.

■ RESULTS AND DISCUSSION

The synthesis of SnO₂ NPs developed in this study is based on the reaction of SnCl₄ with benzyl alcohol. This approach leads to NPs that can be dispersed in organic solvents without the use of any additional stabilizers.⁴⁴ Unlike common alcohols, benzyl alcohol is easier to ionize and undergoes nucleophilic addition due to the direct bonding of the benzene ring with the α -carbon, leading to a more stable carbocation intermediate. The OH⁻ produced by this ionization process is used as an oxygen source for SnO₂ formation, whereas the benzyl carbocation is anchored to the hydroxylated NP surface via an S_N1 reaction mechanism.⁴⁵ The attached benzyl alkoxide groups on the surface of SnO₂ act to stabilize the NPs and prevent aggregation.⁴⁶

In the reaction, SnO₂ NP formation and crystallinity are determined by the reaction temperature. Microwave radiation provides a convenient and economic source of heat generation, provided that the reaction medium can absorb microwave radiation.⁴⁷ We tested neat benzyl alcohol as a reaction solvent. It does enable SnO₂ NP formation but results in difficulties in printing the resulting dispersion into thin films due to the poor drying at desired annealing conditions. As such, we have

focused on a mixed benzyl alcohol and ethanol reaction solution. This mixture enables a rapid increase in heat generation within the microwave reactor (ethanol has a higher OH density) to produce higher crystallinity SnO₂ NPs and supports low-temperature SnO₂ NP printing (*vide infra*).

We first study the effects of microwave heating temperature and duration on the SnO₂ NP size. The particle size and distribution of the reacted mixture were determined through dynamic light scattering (see Figure S1). The peak particle sizes of 5.5, 6.5, and 10 nm are achieved for reactions conducted at 100, 170, and 200 °C, respectively (Figure S1a). A comparable increase in the particle size is also seen when increasing the reaction duration from 10 min to 1 h at 170 °C, yielding 5.6 and 10 nm NPs, respectively (Figure S1b). This increase in average particle size at elevated temperature or reaction duration provides a facile way to fine-tune the final dispersion properties. As a way of focusing the remainder of this study, we assess these SnO₂ NPs as ETLs within Cs_{0.06}FA_{1.11}MA_{0.20}Pb_{1.40}I_{3.55}Br_{0.62} perovskite-based solar cells using the desired printing conditions (i.e., 140 °C for 2 min). The PV data suggest that the ink with an average particle size of 6.5 nm shows the best performance (Figure S2 and Table

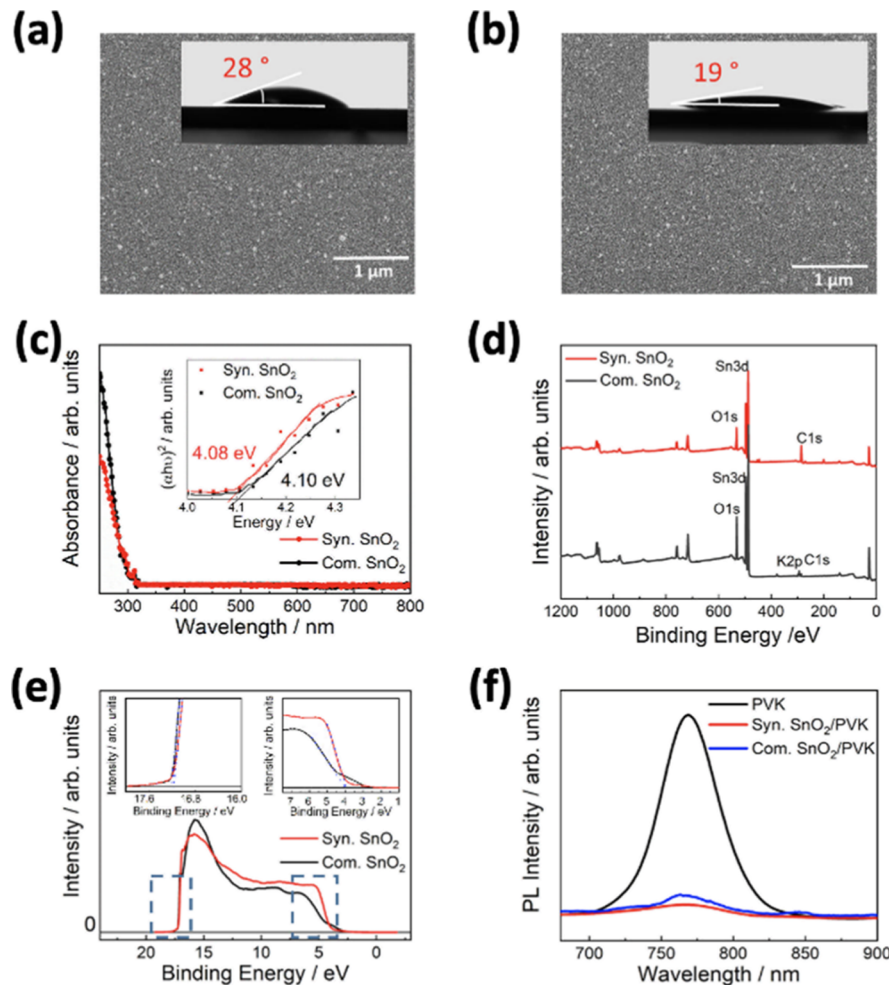


Figure 3. SEM of thin-film coatings made from (a) synthesized and (b) commercial SnO₂ NPs on Si substrates that have been annealed at 140 °C for 2 min. Contact angle measurements of SnO₂ thin films on Si are included as insets. (c) UV-vis absorbance spectra of SnO₂ films on quartz substrates. Inset includes the Tauc plots of the SnO₂ thin films. (d) XPS spectra of synthesized and commercial SnO₂ films deposited by spin coating on ITO at 140 °C. (e) Ultraviolet photoelectron spectroscopy (UPS) spectra of synthesized and commercial SnO₂ films coated on ITO substrates. (f) PL emission spectra of the pristine perovskite and the SnO₂/perovskite films coated on plain glass and excited using 460 nm light from the glass side.

S1). Hence, this ink has been used for further characterization and device optimization.

Given that commercially available aqueous dispersions of SnO₂ NPs represent the state-of-the-art in the field, we quantitatively compare the structural, electronic, and PV characteristics of these commercial dispersions to our benzyl alcohol-based NPs. The TEM micrograph in Figure 2a shows that the best performing, albeit diluted 100-fold, SnO₂ ink possesses oblong-shaped particles. However, analogous measurements of inks diluted by only 10 times with ethanol exhibits more regular, spherically shaped SnO₂ particles of a ~5 nm particle size (Figure S3). This suggests that coarsening or oriented attachment may occur upon dilution. Meanwhile, the size of water-based commercial SnO₂ NPs was 4 nm (Figure 2b). The defined selected area electron diffraction (SAED) patterns confirm the crystalline nature of both SnO₂ NPs (inset of Figure 2a,b). The phase and structural purity of the SnO₂ NPs were studied by XRD. The diffractograms of synthesized and commercial SnO₂ NPs are shown in Figure 2c. The prominent peaks at (110), (101), (200), (211), and (002) confirm the formation of tetragonal SnO₂ (indexed in JCPDS card no. 41-1445), which is similar to the commercial SnO₂.⁴⁸

The absence of impurity diffraction peaks confirms that there are no crystalline by-products formed during the synthesis. The broad diffraction peaks further indicate the small crystalline nature of the SnO₂ particles, with Scherrer analysis yielding crystal grain sizes for the synthesized and commercial SnO₂ of ~4 and ~3.5 nm, respectively.⁴⁹

Understanding the processing temperature regimes of the developed SnO₂ ink is important for its use in R2R coating. Figure 2d shows the thermogravimetric analysis (TGA) and its derivative plots for both synthesized and commercial SnO₂ NPs. A weight loss of about 3% is observed between 25 and 110 °C for synthesized SnO₂, which is most likely due to the evaporation of residual ethanol (T_b —78 °C) and water (T_b —100 °C). A secondary weight loss of about 8% between 110 and 280 °C is related to the removal of benzyl alkoxide ligands from the surface of SnO₂ (vide infra). Based on the corresponding mass loss in this temperature regime, the benzyl alkoxide ligand density is estimated to be ~4 ligands/nm², which represents a surface coverage of approximately ~80% (see Supporting Information). The final mass loss at a peak temperature of 460 °C is considered to arise from the release of residual chlorides or condensation due to grain

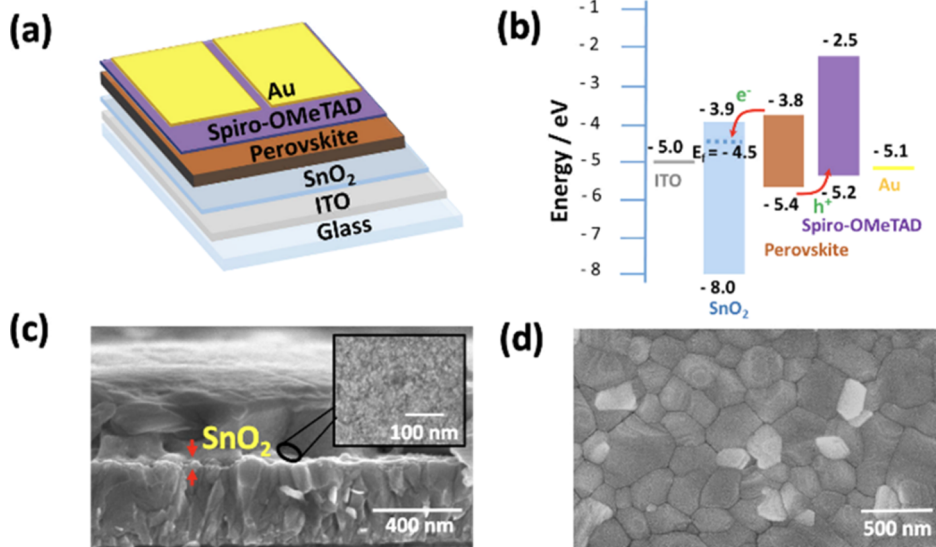


Figure 4. (a) Schematic of the device structure. (b) Energy band diagram of the individual materials used within the PSC, showing the separation and collection of photo-generated electrons and holes. The energy values of the SnO_2 were obtained from the combination of UPS and optical absorption measurements. (c) Cross-sectional image of FTO/spin-coated SnO_2 /perovskite/spiro-OMeTAD (inset—top-view of the SnO_2 film on FTO) and (d) surface morphology of the perovskite film deposited on SnO_2 .

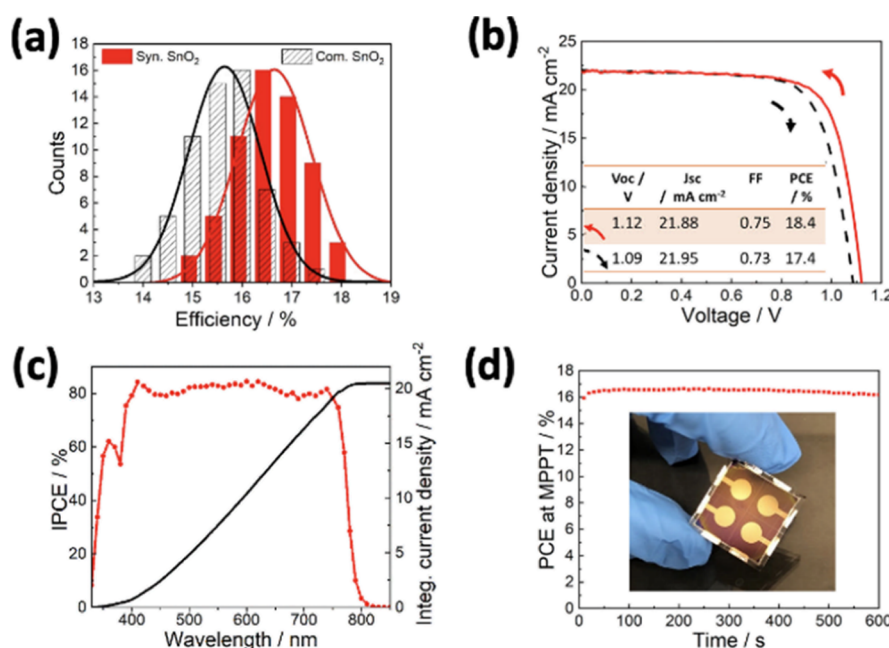


Figure 5. (a) PCE distribution of ~ 50 individual PSCs based on the reverse scan. (b) $J-V$ characteristics of the champion PSCs fabricated using a spin-coated SnO_2 ETL that was annealed at 140°C for 2 min. (c) IPCE and the integrated current density plots of this champion PSC and (d) PCE as a function of time at MPP tracking of an average performing device with SnO_2 as ETL.

growth at the higher temperatures (Figure S4).^{50–52} In comparison, the water-based commercial sample exhibited a total mass loss of 10% between 25 and 700°C . This was composed of a dominant weight-loss event between 90 and 110°C , which can be directly attributed to residual or adsorbed water being removed, and a subsequent gradual reduction between 200 and 700°C , likely due to condensation between the particles themselves. Based on the TGA, the total solid loading of the synthesized and commercial SnO_2 inks was calculated to be 130 and 140 mg/mL, respectively.

To understand the chemistry presented in the benzyl alcohol-synthesized and commercial SnO_2 NP thin films, we

carried out FTIR on films annealed at different temperatures (Figure 2e,f). The IR signatures in the range of $700\text{--}500\text{ cm}^{-1}$ in both cases correspond to the antisymmetric $\text{Sn}-\text{O}$ stretching and symmetric $\text{Sn}-\text{O}-\text{Sn}$ stretching vibrations, confirming the presence of SnO_2 .⁵³ Furthermore, the broad band in the range of $3500\text{--}3200\text{ cm}^{-1}$ is assigned to $\text{O}-\text{H}$ stretching in both samples. A clear decrease in these stretches with an increased temperature indicates that dehydration occurs at elevated temperatures. For the sample prepared in benzyl alcohol, additional aliphatic and aromatic C–H stretching peaks are seen between 2800 and 3200 cm^{-1} , confirming the presence of the benzyl alkoxide ligands.⁵⁴ When

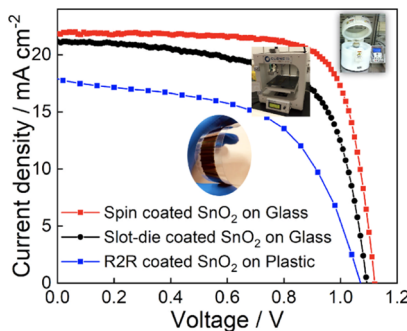


Figure 6. Best J – V characteristics of PSCs using spin-coated, slot die-coated, and R2R-coated SnO_2 ETLs annealed at 140 °C for 2 min (compared to the reverse scans of the JV curves).

the annealing temperature rises from 80 to 240 °C, residual ethanol, water, and surface-bound benzyl alkoxide ligands are progressively removed, as evident from TGA. Notably, at our targeted processing temperature of 140 °C, clear evidence of benzyl alkoxide ligands remains on the SnO_2 NPs.

The SEM images of spin-coated SnO_2 thin films on Si substrates show homogeneous surface coatings from synthesized (Figure 3a) and commercial (Figure 3b) dispersions. Given the importance of wettability during R2R printing, the water contact angle on different SnO_2 thin films was also measured. A contact angle of $\sim 28 \pm 3^\circ$ (inset of Figure 3a) was measured for the synthesized SnO_2 film, whereas a lower value of $19 \pm 1^\circ$ was observed for the commercial SnO_2 film (inset of Figure 3b). The higher water contact angle of our synthesized SnO_2 is consistent with the presence of benzyl alkoxide groups, imparting hydrophobicity to the thin-film surface.

To probe the optical properties of the SnO_2 NP thin films, UV–vis absorption spectra were obtained by performing the transmission and reflection measurements of the films coated on quartz substrates using an integrating sphere (Figure 3c). The results show negligible absorption across the entire visible region, with Tauc plots indicating comparable optical band gaps of ~ 4.1 eV in both samples. This is slightly higher than the band gap of ~ 3.6 eV for bulk SnO_2 ,⁵⁵ which can be partly explained by dielectric or quantum confinement effects owing to the SnO_2 NPs being close to the effective Bohr radius of 2.7 nm.⁵⁶ Notably, this blue shift in SnO_2 absorption is potentially useful for solar application as it decreases parasitic absorption within the ETL.⁵⁷

The surface chemical composition of synthesized and commercial SnO_2 films was determined by XPS. Figures 3d and S5 show the XPS survey scan and narrow scan of SnO_2 films deposited by spin coating at 140 °C on ITO glass substrates, respectively. High-resolution valence-band spectra were used for charge correction and are shown in Figure S4e. The two peaks observed at ~ 486 and ~ 495 eV in Figure S4e are ascribed to $\text{Sn} 3\text{d}^{5/2}$ and $\text{Sn} 3\text{d}^{3/2}$, respectively, occurring from Sn^{4+} .⁵⁸ For both the samples, the splitting between the Sn

3d doublet was found to be ~ 8.4 eV, which is consistent with that reported for SnO_2 and the presence of $\text{Sn}(\text{IV})$ states.⁵⁹ The O1s core line (Figure S5b,c) is decomposed to identify different oxygen chemical states.⁴³ The O 1s peak at lower binding energy at ~ 530 eV corresponds to oxygen bonded to the Sn atoms, and the peak at higher binding energy at ~ 531 eV corresponds to oxygen-induced vacancies.^{43,60} Figure S4d compares the C 1s signatures of the different SnO_2 thin films, showing aromatic and aliphatic carbon from the synthesized and commercial samples, respectively. The former is consistent with the benzyl alcohol surface chemistry of the synthesized SnO_2 , while the latter arises from adventitious carbon impurities. Finally, another key difference across the samples is that the commercial SnO_2 has potassium, which has been previously reported in the literature.¹⁹

The UPS data of the SnO_2 thin film coated on FTO are presented in Figure 3e. From the spectrum, the valence-band edge and secondary electron cut-off binding energy of SnO_2 are determined by extrapolating the leading edge of the spectrum to the baseline. Based on the UPS measurements, the valence-band energies for the synthesized and commercial SnO_2 are determined to be -7.95 ± 0.05 and -7.91 ± 0.1 eV, respectively. With the E_g values obtained from absorption measurements, the conduction-band-minimum energy levels for these systems are recorded as -3.87 ± 0.15 and -3.81 ± 0.15 eV for synthesized and commercial SnO_2 , respectively. Meanwhile, the Fermi levels were determined to be -4.5 and -4.4 eV, respectively. While these values represent comparable electronic properties of the energy band levels,⁶¹ the commercial SnO_2 thin film does exhibit a well-defined shoulder on the low binding energy (Figure 3e—top right inset). This is indicative of sub-gap valence-band states, which generally hinder charge transport and result in poorer device performance.⁶²

AFM was conducted to gauge the topographies of the spin-coated SnO_2 thin films with and without annealing (Figure S6), as well as for varying SnO_2 ink concentrations by changing the SnO_2/IPA ratio (Figure S7). The film morphologies and roughness were not changed significantly through either annealing or concentration modifications (RMS ~ 2.5 – 2.8 nm). When compared to commercial SnO_2 films (Figure S8, RMS ~ 1.9 – 2.1 nm), a slightly higher roughness was observed for our synthesized SnO_2 films.

Figure 3f shows the PL emission spectra of the pristine perovskite film on glass and on synthesized and commercial SnO_2 . While both interfaces demonstrate effective (electron) quenching from the perovskite, the slight enhancement in quenching of the synthesized SnO_2 is suggestive of improved charge transfer. This factor is consistent with topography measurements, where an increase in the contact area between the active layer and the ETL layer can improve charge extraction.⁶³

The usability of the synthesized SnO_2 as an ETL in PSCs is demonstrated by constructing n–i–p planar structured FTO/

Table 1. Champion and Average (20 Devices) Device Performance along with the Hysteresis Index (HI) of the PSCs Made by Spin-Coated, Slot Die-Coated, and R2R-Coated SnO_2

SnO_2 coating method	V_{oc}/V	$J_{\text{sc}}/\text{mA cm}^{-2}$	FF	PCE/%	HI/%
spin coating on glass subs	1.12 (1.11 ± 0.01)	21.88 (21.72 ± 0.06)	0.75 (0.74 ± 0.01)	18.40 (17.87 ± 0.34)	5
slot-die coating on glass subs	1.12 (1.11 ± 0.01)	21.21 (21.04 ± 0.25)	0.66 (0.66 ± 0.01)	15.30 (15.07 ± 0.16)	5
R2R coating on flexible subs	1.07 (1.07 ± 0.01)	17.36 (17.19 ± 0.20)	0.56 (0.55 ± 0.01)	10.40 (10.12 ± 0.31)	6

$\text{SnO}_2/\text{Cs}_{0.06}\text{FA}_{1.11}\text{MA}_{0.20}\text{Pb}_{1.40}\text{I}_{3.55}\text{Br}_{0.62}$ /spiro-OMeTAD/Au PSCs (Figure 4a). Figure 4b illustrates the favorable energy alignment between each of the layers forming this PSC structure. Initially, the SnO_2 ETL was fabricated on conducting glass substrates by spin coating using a diluted SnO_2 dispersion in IPA followed by annealing at 140 °C for 2 min in air. Here, the post-annealing temperature and duration of the SnO_2 ETL were the same as the processing conditions used for R2R processing. From direct current–voltages measurements, the films exhibited average conductivities of $3.1 \times 10^{-6} \text{ S/cm}$ (Figure S10 and Table S2). The SEM image in Figure 4c shows that the thickness of the SnO_2 ETL is ~30 nm and supports the formation of a highly conformal interface between the SnO_2 NPs and the perovskite layer. The quality of the perovskite films, including grain size, crystallinity, and surface coverage, is greatly influenced by the uniformity of the ETL in the n–i–p device structure.⁶⁴ Figure 4d shows the surface morphology of the perovskite film deposited on the synthesized SnO_2 layer. The image attests that the perovskite film formed is continuous and pinhole-free, with an average grain size of about 300 nm. Importantly, similar results are obtained for slot die-coated SnO_2 NP films shown in Figure S9. This indicates comparable film properties across both deposition methods.

Photovoltaic measurements were conducted to evaluate the performance of SnO_2 as the ETL using the aforementioned device architecture. Figure S11 and Table S3 compare the PV performance of PSCs made using synthesized and commercial SnO_2 NPs as ETLs that are processed under different annealing temperatures for 2 min. The results indicate that the annealing of our synthesized SnO_2 film at 140 °C for 2 min helps us to increase the device performance from 16.6% (RT processing) to 17.8%. This likely arises from the removal of residual ethanol and water to improve the interfacial properties of the perovskite. However, further increasing the annealing temperature up to 240 °C did not change the device performance significantly, indicating that annealing at 140 °C for 2 min is sufficient to yield a high-quality SnO_2 ETL. Conversely, the devices made using the water-based commercial SnO_2 ink showed an improvement in the device performance (from 16.4 to 17.1%) when increasing the annealing temperature from 140 to 240 °C. This indicates that annealing the commercial SnO_2 ETL at higher temperatures for a shorter time (240 °C for 2 min) is necessary to optimize the film properties for use in PSCs.

Figure 5a shows a PCE histogram for over 50 devices fabricated using synthesized SnO_2 and commercial SnO_2 as ETLs were processed at 140 °C for 2 min. The histogram indicates that an enhancement in the PCE of the devices made using synthesized SnO_2 ETL compared to the commercial SnO_2 from 15.7 to 16.8% is observed. This improved PCE of the SnO_2 ETL-based PSCs is attributed to the good charge extraction properties of SnO_2 , together with the uniform thickness and homogeneous morphology of the ETL and the perovskite layer, leading to minor charge losses at the interface. Figure 5b shows the best current density–voltage (J – V) curve recorded for the PSC made using SnO_2 ETL prepared by annealing the spin-coated SnO_2 on FTO at 140 °C for 2 min. The forward scan showed 17.4% photo-conversion efficiency (PCE), whereas the reverse scan demonstrated 18.4% device efficiency with a V_{oc} of 1.12 V, J_{sc} of 21.88 mA cm^{-2} , and a fill factor of 0.75. To the best of our knowledge, this is among the best-reported PSC efficiencies achieved to date for a planar

SnO_2 ETL deposited using a low-temperature solution process with a short annealing step (i.e., 140 °C for 2 min). The IPCE of the device was measured, and the derived integrated current density (20.8 mA/cm^2) is in good agreement (<5% deviation) with the J_{sc} value obtained from the J – V curve measured under the AM 1.5G light source (Figure 5c). Short term maximum power point (MPP) stability of the device tested under steady-state illumination conditions without any encapsulation showed no dramatic changes over the testing period of 600 s (Figure 5d).

Our main intention of developing this low-temperature processable SnO_2 ink is to use it in fabricating the ETL in large-scale printed PSC modules. Thus, we constructed PSCs using slot die-coated SnO_2 ETLs with the developed ink. Post-annealing of the slot-die coated SnO_2 film was performed at 140 °C for 2 min to mimic the typical R2R processing conditions (Figure S12). The other layers of the device were fabricated by spin coating. Figure 6 compares the best reverse J – V scans of the devices made using spin, slot-die, and R2R-coated SnO_2 ETLs. The best PCE of 15.3% with V_{oc} of 1.12 V, J_{sc} of 21.21 mA cm^{-2} , and a fill factor of 0.66 was achieved for a PSC with slot die-coated SnO_2 . Furthermore, we also tested the applicability of using the developed SnO_2 ink in fabricating a SnO_2 ETL on flexible ITO substrates by the R2R printing technique. Similarly, flexible PSCs were constructed by coating SnO_2 ETL on ITO plastic substrates using the developed ink by the R2R process. The remaining layers of the device were fabricated by spin coating. For this R2R-coated SnO_2 -based flexible PSC, we achieved the highest PCE of 10.4% (Table 1). This provides an important first step toward demonstrating the prospects of our SnO_2 ink in printing n–i–p structured PSC modules on plastic substrates by a R2R coating technique, with further studies underway to realize its use in fully printed PSCs on flexible substrates.

CONCLUSIONS

In conclusion, we report a facile and scalable microwave-assisted synthesis of SnO_2 nanocrystal inks that can be directly used without purification in fabricating SnO_2 thin films on glass or plastic substrates at low temperatures. By utilizing a benzyl alcohol/ethanol solvent mixture, this one-pot method enables colloidally stable SnO_2 nanocrystals with a controllable size of between 5 and 10 nm and benzyl alkoxide surface stabilization to be synthesized. These nanocrystal dispersions can be readily deposited as thin films without any purification steps and have been demonstrated as effective electron transport layers within PSCs. For ETLs fabricated using spin-coating and thermally annealed at only 140 °C for 2 min, PSCs with an efficiency of over 18% have been realized. In comparison, devices made with commercial (aqueous) SnO_2 NP inks under these low-temperature and short thermal annealing conditions achieved champion devices of only 16.2%. Meanwhile, comparable devices were fabricated using slot die-coated SnO_2 ETLs on glass substrates and plastic substrates by R2R printing to yield devices with efficiencies of 15.3 and 10.4%, respectively. While further optimization opportunities will undoubtedly lend themselves to further efficiency enhancements; these results demonstrate the suitability of the developed SnO_2 ink to be widely used for both spin-coating and R2R printing approaches. This versatility will support the more ready translation of results obtained from small-scale prototypes to the large-scale production of PSC modules.

■ ASSOCIATED CONTENT

§ Supporting Information

The Supporting Information is available free of charge at <https://pubs.acs.org/doi/10.1021/acs.chemmater.2c00578>.

Additional characterization of the commercial and synthesized SnO₂ particles, including dynamical light scattering; XRD; XPS; conductivity and AFM; solar cell current–voltage measurements; and ligand surface coverage calculations ([PDF](#))

Slot-die coating of the synthesised SnO₂ ink on ITO-coated PET ([MP4](#))

■ AUTHOR INFORMATION

Corresponding Author

Jacek J. Jasieniak – ARC Centre of Excellence in Exciton Science, Department of Materials Science and Engineering, Faculty of Engineering, Monash University, Clayton, Victoria 3800, Australia;  orcid.org/0000-0002-1608-6860; Email: jacek.jasieniak@monash.edu

Authors

T. A. Nirmal Peiris – ARC Centre of Excellence in Exciton Science, Department of Materials Science and Engineering, Faculty of Engineering, Monash University, Clayton, Victoria 3800, Australia

Hasitha C. Weerasinghe – CSIRO Manufacturing, Clayton, Victoria 3168, Australia

Manoj Sharma – ARC Centre of Excellence in Exciton Science, Department of Materials Science and Engineering, Faculty of Engineering, Monash University, Clayton, Victoria 3800, Australia;  orcid.org/0000-0001-5215-9740

Jueng-Eun Kim – ARC Centre of Excellence in Exciton Science, Department of Materials Science and Engineering, Faculty of Engineering, Monash University, Clayton, Victoria 3800, Australia

Monika Michalska – ARC Centre of Excellence in Exciton Science, Department of Materials Science and Engineering, Faculty of Engineering, Monash University, Clayton, Victoria 3800, Australia;  orcid.org/0000-0002-8376-7738

Naresh Chandrasekaran – ARC Centre of Excellence in Exciton Science, Department of Materials Science and Engineering, Faculty of Engineering, Monash University, Clayton, Victoria 3800, Australia;  orcid.org/0000-0001-5473-8068

Dimuthu C. Senevirathna – ARC Centre of Excellence in Exciton Science, Department of Materials Science and Engineering, Faculty of Engineering, Monash University, Clayton, Victoria 3800, Australia

Hanchen Li – ARC Centre of Excellence in Exciton Science, Department of Materials Science and Engineering, Faculty of Engineering, Monash University, Clayton, Victoria 3800, Australia;  orcid.org/0000-0001-6626-5894

Anthony S. R. Chesman – CSIRO Manufacturing, Clayton, Victoria 3168, Australia;  orcid.org/0000-0002-1807-4468

Doojin Vak – CSIRO Manufacturing, Clayton, Victoria 3168, Australia;  orcid.org/0000-0001-7704-5563

Complete contact information is available at:

<https://pubs.acs.org/doi/10.1021/acs.chemmater.2c00578>

Funding

This work was funded predominantly by the Australian Renewable Energy Agency (2017/RND012) and with minor contributions from the Australian Research Council Center of Excellence in Exciton Science (grant no. CE170100026). This research used equipment funded by the Australian Research Council grant LE130100072.

Notes

The authors declare no competing financial interest.

■ ACKNOWLEDGMENTS

The authors acknowledge the use of facilities within the Monash X-ray Platform (MXP), the Monash Centre for Electron Microscopy (MCEM). We would also like to acknowledge Dr. Chris Easton from CSIRO on his invaluable guidance in interpreting the XPS. We would also like to thank Dr Tom Raeber at CSIRO for conducting the AFM measurements.

■ REFERENCES

- (1) Tai, Q.; Tang, K.-C.; Yan, F. Recent Progress of Inorganic Perovskite Solar Cells. *Energy Environ. Sci.* **2019**, *12*, 2375–2405.
- (2) Jung, Y.-S.; Hwang, K.; Heo, Y.-J.; Kim, J.-E.; Vak, D.; Kim, D.-Y. Progress in Scalable Coating and Roll-to-Roll Compatible Printing Processes of Perovskite Solar Cells toward Realization of Commercialization. *Adv. Opt. Mater.* **2018**, *6*, 1701182.
- (3) NREL. Best Research-Cell Efficiency Chart. <https://www.nrel.gov/pv/cell-efficiency.html> (accessed Oct 26, 2020).
- (4) Jiang, Q.; Zhao, Y.; Zhang, X.; Yang, X.; Chen, Y.; Chu, Z.; Ye, Q.; Li, X.; Yin, Z.; You, J. Surface Passivation of Perovskite Film for Efficient Solar Cells. *Nat. Photonics* **2019**, *13*, 460–466.
- (5) Galagan, Y.; Di Giacomo, F.; Gorter, H.; Kirchner, G.; de Vries, I.; Andriessen, R.; Groen, P. Roll-to-Roll Slot Die Coated Perovskite for Efficient Flexible Solar Cells. *Adv. Energy Mater.* **2018**, *8*, 1801935.
- (6) Kim, Y. Y.; Yang, T. Y.; Suhonen, R.; Välimäki, M.; Maaninen, T.; Kemppainen, A.; Jeon, N. J.; Seo, J. Gravure-Printed Flexible Perovskite Solar Cells: Toward Roll-to-Roll Manufacturing. *Adv. Sci.* **2019**, *6*, 1802094.
- (7) Yang, D.; Yang, R.; Priya, S.; Liu, S. F. Recent Advances in Flexible Perovskite Solar Cells: Fabrication and Applications. *Angew. Chem., Int. Ed.* **2019**, *58*, 4466–4483.
- (8) Madogni, V. I.; Kounouhéwa, B.; Akpo, A.; Agbomahéna, M.; Hounkpatin, S. A.; Awanou, C. N. Comparison of Degradation Mechanisms in Organic Photovoltaic Devices upon Exposure to a Temperate and a Subequatorial Climate. *Chem. Phys. Lett.* **2015**, *640*, 201–214.
- (9) Shin, S. S.; Lee, S. J.; Seok, S. I. Metal Oxide Charge Transport Layers for Efficient and Stable Perovskite Solar Cells. *Adv. Funct. Mater.* **2019**, *29*, 1900455.
- (10) Peiris, T. A. N.; Baranwal, A. K.; Kanda, H.; Fukumoto, S.; Kanaya, S.; Cojocaru, L.; Bessho, T.; Miyasaka, T.; Segawa, H.; Ito, S. Enhancement of the Hole Conducting Effect of NiO by a N2 Blow Drying Method in Printable Perovskite Solar Cells with Low-Temperature Carbon as the Counter Electrode. *Nanoscale* **2017**, *9*, 5475–5482.
- (11) Baranwal, A. K.; Kanaya, S.; Peiris, T. A. N.; Mizuta, G.; Nishina, T.; Kanda, H.; Miyasaka, T.; Segawa, H.; Ito, S. 100 °C Thermal Stability of Printable Perovskite Solar Cells Using Porous Carbon Counter Electrodes. *ChemSusChem* **2016**, *9*, 2604–2608.
- (12) Mahmood, K.; Sarwar, S.; Mehran, M. T. Current Status of Electron Transport Layers in Perovskite Solar Cells: Materials and Properties. *RSC Adv.* **2017**, *7*, 17044–17062.
- (13) Wilkes, G. C.; Deng, X.; Choi, J. J.; Gupta, M. C. Laser Annealing of TiO2 Electron-Transporting Layer in Perovskite Solar Cells. *ACS Appl. Mater. Interfaces* **2018**, *10*, 41312–41317.
- (14) Ke, W.; Fang, G.; Liu, Q.; Xiong, L.; Qin, P.; Tao, H.; Wang, J.; Lei, H.; Li, B.; Wan, J.; Yang, G.; Yan, Y. Low-Temperature Solution-

- Processed Tin Oxide as an Alternative Electron Transporting Layer for Efficient Perovskite Solar Cells. *J. Am. Chem. Soc.* **2015**, *137*, 6730–6733.
- (15) Jiang, Q.; Zhang, X.; You, J. SnO₂: A Wonderful Electron Transport Layer for Perovskite Solar Cells. *Small* **2018**, *14*, 1801154.
- (16) Liu, H.; Chen, Z.; Wang, H.; Ye, F.; Ma, J.; Zheng, X.; Gui, P.; Xiong, L.; Wen, J.; Fang, G. A Facile Room Temperature Solution Synthesis of SnO₂ Quantum Dots for Perovskite Solar Cells. *J. Mater. Chem. A* **2019**, *7*, 10636–10643.
- (17) Bu, T.; Shi, S.; Li, J.; Liu, Y.; Shi, J.; Chen, L.; Liu, X.; Qiu, J.; Ku, Z.; Peng, Y.; Zhong, J.; Cheng, Y.-B.; Huang, F. Low-Temperature Presynthesized Crystalline Tin Oxide for Efficient Flexible Perovskite Solar Cells and Modules. *ACS Appl. Mater. Interfaces* **2018**, *10*, 14922–14929.
- (18) Yang, D.; Yang, R.; Wang, K.; Wu, C.; Zhu, X.; Feng, J.; Ren, X.; Fang, G.; Priya, S.; Liu, S. F. High Efficiency Planar-Type Perovskite Solar Cells with Negligible Hysteresis Using EDTA-Complexed SnO₂. *Nat. Commun.* **2018**, *9*, 3239.
- (19) Bu, T.; Li, J.; Zheng, F.; Chen, W.; Wen, X.; Ku, Z.; Peng, Y.; Zhong, J.; Cheng, Y.-B.; Huang, F. Universal Passivation Strategy to Slot-Die Printed SnO₂ for Hysteresis-Free Efficient Flexible Perovskite Solar Module. *Nat. Commun.* **2018**, *9*, 4609.
- (20) Méndez, P. F.; Muhammed, S. K. M.; Barea, E. M.; Masi, S.; Mora-Seró, I. Analysis of the UV Ozone-Treated SnO₂ Electron Transporting Layer in Planar Perovskite Solar Cells for High Performance and Reduced Hysteresis. *Sol. RRL* **2019**, *3*, 1900191.
- (21) Waqas Alam, M.; Khatoon, U.; Qurashi, A. Synthesis and Characterization of Cu-SnO₂ Nanoparticles Deposited on Glass Using Ultrasonic Spray Pyrolysis and Their H₂S Sensing Properties. *Curr. Nanosci.* **2012**, *8*, 919–924.
- (22) Suthakaran, S.; Dhanapandian, S.; Krishnakumar, N.; Ponpandian, N. Hydrothermal Synthesis of SnO₂ Nanoparticles and Its Photocatalytic Degradation of Methyl Violet and Electrochemical Performance. *Mater. Res. Express* **2019**, *6*, 0850i3.
- (23) Li, Y.; Peng, R.; Xiu, X.; Zheng, X.; Zhang, X.; Zhai, G. Growth of SnO₂ Nanoparticles via Thermal Evaporation Method. *Superlattices Microstruct.* **2011**, *50*, 511–516.
- (24) Deepa, K.; Venkatesha, T. V. Combustion Synthesis of Ni Doped SnO₂ Nanoparticles for Applications in Zn-Composite Coating on Mild Steel. *J. Sci.: Adv. Mater. Devices* **2018**, *3*, 412–418.
- (25) Aziz, M.; Saber Abbas, S.; Wan Baharom, W. R. Size-Controlled Synthesis of SnO₂ Nanoparticles by Sol-Gel Method. *Mater. Lett.* **2013**, *91*, 31–34.
- (26) Chen, W.; Ghosh, D.; Chen, S. Large-Scale Electrochemical Synthesis of SnO₂ Nanoparticles. *J. Mater. Sci.* **2008**, *43*, 5291–5299.
- (27) Wang, J.; Lian, G.; Si, H.; Wang, Q.; Cui, D.; Wong, C.-P. Pressure-Induced Oriented Attachment Growth of Large-Size Crystals for Constructing 3D Ordered Superstructures. *ACS Nano* **2016**, *10*, 405–412.
- (28) Ma, N.; Suematsu, K.; Yuasa, M.; Kida, T.; Shimano, K. Effect of Water Vapor on Pd-Loaded SnO₂ Nanoparticles Gas Sensor. *ACS Appl. Mater. Interfaces* **2015**, *7*, 5863–5869.
- (29) Xu, X.; Zhuang, J.; Wang, X. SnO₂ Quantum Dots and Quantum Wires: Controllable Synthesis, Self-Assembled 2D Architectures, and Gas-Sensing Properties. *J. Am. Chem. Soc.* **2008**, *130*, 12527–12535.
- (30) Jiang, L.; Sun, G.; Zhou, Z.; Sun, S.; Wang, Q.; Yan, S.; Li, H.; Tian, J.; Guo, J.; Zhou, B.; Xin, Q. Size-Controllable Synthesis of Monodispersed SnO₂ Nanoparticles and Application in Electrocatalysts. *J. Phys. Chem. B* **2005**, *109*, 8774–8778.
- (31) Fujihara, S.; Maeda, T.; Ohgi, H.; Hosono, E.; Imai, H.; Kim, S.-H. Hydrothermal Routes to Prepare Nanocrystalline Mesoporous SnO₂ Having High Thermal Stability. *Langmuir* **2004**, *20*, 6476–6481.
- (32) Xu, Z.; Jiang, Y.; Li, Z.; Chen, C.; Kong, X.; Chen, Y.; Zhou, G.; Liu, J.-M.; Kempa, K.; Gao, J. Rapid Microwave-Assisted Synthesis of SnO₂ Quantum Dots for Efficient Planar Perovskite Solar Cells. *ACS Appl. Energy Mater.* **2021**, *4*, 1887–1893.
- (33) Ghanizadeh, S.; Peiris, T. A. N.; Jayathilake, D. S. Y.; Hutt, D. A.; Wijayantha, K. G. U.; Southee, D. J.; Conway, P. P.; Marchand, P.; Darr, J. A.; Parkin, I. P.; Carmalt, C. J. Dispersion and Microwave Processing of Nano-Sized ITO Powder for the Fabrication of Transparent Conductive Oxides. *Ceram. Int.* **2016**, *42*, 18296–18302.
- (34) Bhatti, I. A.; Nirmal Peiris, T. A.; Smith, T. D.; Upul Wijayantha, K. G. Hierarchical ZnO Nanorod Electrodes: Effect of Post Annealing on Structural and Photoelectrochemical Performance. *Mater. Lett.* **2013**, *93*, 333–336.
- (35) Abulikemu, M.; Neophytou, M.; Barbé, J. M.; Tietze, M. L.; El Labban, A.; Anjum, D. H.; Amassian, A.; McCulloch, I.; Del Gobbo, S. Microwave-Synthesized Tin Oxide Nanocrystals for Low-Temperature Solution-Processed Planar Junction Organo-Halide Perovskite Solar Cells. *J. Mater. Chem. A* **2017**, *5*, 7759–7763.
- (36) Srivastava, A.; Lakshmikumar, S. T.; Srivastava, A. K.; Rashmi; Jain, K. Gas Sensing Properties of Nanocrystalline SnO₂ Prepared in Solvent Media Using a Microwave Assisted Technique. *Sens. Actuators, B* **2007**, *126*, 583–587.
- (37) Krishnakumar, T.; Jayaprakash, R.; Parthibavarman, M.; Phani, A. R.; Singh, V. N.; Mehta, B. R. Microwave-Assisted Synthesis and Investigation of SnO₂ Nanoparticles. *Mater. Lett.* **2009**, *63*, 896–898.
- (38) Asdim, A.; Manseki, K.; Sugiura, T.; Yoshida, T. Microwave Synthesis of Size-Controllable SnO₂ Nanocrystals for Dye-Sensitized Solar Cells. *New J. Chem.* **2014**, *38*, 598–603.
- (39) Jayathilake, D. S. Y.; Peiris, T. A. N.; Sagu, J. S.; Potter, D. B.; Wijayantha, K. G. U.; Carmalt, C. J.; Southee, D. J. Microwave-Assisted Synthesis and Processing of Al-Doped, Ga-Doped, and Al, Ga Codoped ZnO for the Pursuit of Optimal Conductivity for Transparent Conducting Film Fabrication. *ACS Sustainable Chem. Eng.* **2017**, *5*, 4820–4829.
- (40) Nirmal Peiris, T. A. Microwave-Assisted Processing of Solid Materials for Sustainable Energy Related Electronic and Optoelectronic Applications. Ph.D. Thesis, Loughborough University, 2014.
- (41) Garnweitner, G.; Niederberger, M. Nonaqueous and Surfactant-Free Synthesis Routes to Metal Oxide Nanoparticles. *J. Am. Ceram. Soc.* **2006**, *89*, 1801–1808.
- (42) Hayashi, Y. Pot Economy and One-Pot Synthesis. *Chem. Sci.* **2016**, *7*, 866–880.
- (43) Kwoka, M.; Krzywiecki, M. Impact of Air Exposure and Annealing on the Chemical and Electronic Properties of the Surface of SnO₂ Nanolayers Deposited by Rheotaxial Growth and Vacuum Oxidation. *Beilstein J. Nanotechnol.* **2017**, *8*, 514–521.
- (44) Neri, G.; Bonavita, A.; Rizzo, G.; Galvagno, S.; Pinna, N.; Niederberger, M.; Capone, S.; Siciliano, P. Towards Enhanced Performances in Gas Sensing: SnO₂ Based Nanocrystalline Oxides Application. *Sens. Actuators, B* **2007**, *122*, 564–571.
- (45) Hu, M.; Xu, J.; Gao, J.; Yang, S.; Wong, J. S. P.; Li, R. K. Y. Benzyl Alcohol-Based Synthesis of Oxide Nanoparticles: The Perspective of SN1 Reaction Mechanism. *Dalton Trans.* **2013**, *42*, 9777–9784.
- (46) Deshmukh, R.; Niederberger, M. Mechanistic Aspects in the Formation, Growth and Surface Functionalization of Metal Oxide Nanoparticles in Organic Solvents. *Chem.—Eur. J.* **2017**, *23*, 8542–8570.
- (47) Dąbrowska, S.; Chudoba, T.; Wojnarowicz, J.; Łojkowski, W. Current Trends in the Development of Microwave Reactors for the Synthesis of Nanomaterials in Laboratories and Industries: A Review. *Crystals* **2018**, *8*, 379.
- (48) Cojocaru, L.; Olivier, C.; Toupane, T.; Sellier, E.; Hirsch, L. Size and Shape Fine-Tuning of SnO₂ Nanoparticles for Highly Efficient and Stable Dye-Sensitized Solar Cells. *J. Mater. Chem. A* **2013**, *1*, 13789–13799.
- (49) Lu, X.; Wang, H.; Wang, Z.; Jiang, Y.; Cao, D.; Yang, G. Room-Temperature Synthesis of Colloidal SnO₂ Quantum Dot Solution and Ex-Situ Deposition on Carbon Nanotubes as Anode Materials for Lithium Ion Batteries. *J. Alloys Compd.* **2016**, *680*, 109–115.
- (50) Han, K.; Peng, X.-L.; Li, F.; Yao, M.-M. SnO₂ Composite Films for Enhanced Photocatalytic Activities. *Catalysts* **2018**, *8*, 453.

- (51) Tang, W.; Wang, J.; Yao, P. J.; Du, H. Y.; Sun, Y. H. Preparation, Characterization and Gas Sensing Mechanism of ZnO-Doped SnO₂ Nanofibers. *Acta Phys.-Chim. Sin.* **2014**, *30*, 781–788.
- (52) Gheonea, R.; Mak, C.; Crasmareanu, E. C.; Simulescu, V.; Plesu, N.; Ilia, G. Surface Modification of SnO₂ with Phosphonic Acids. *J. Chem.* **2017**, *2017*, 2105938.
- (53) Kumar, A.; Rout, L.; Dhaka, R. S.; Samal, S. L.; Dash, P. Design of a Graphene Oxide-SnO₂ Nanocomposite with Superior Catalytic Efficiency for the Synthesis of β -Enaminones and β -Enaminoesters. *RSC Adv.* **2015**, *5*, 39193–39204.
- (54) Baek, S.; Yu, S.-H.; Park, S.-K.; Pucci, A.; Marichy, C.; Lee, D.-C.; Sung, Y.-E.; Piao, Y.; Pinna, N. A One-Pot Microwave-Assisted Non-Aqueous Sol-Gel Approach to Metal Oxide/Graphene Nano-composites for Li-Ion Batteries. *RSC Adv.* **2011**, *1*, 1687–1690.
- (55) Das, S.; Jayaraman, V. SnO₂: A comprehensive review on structures and gas sensors. *Prog. Mater. Sci.* **2014**, *66*, 112–255.
- (56) Shaalan, N. M.; Hamad, D.; Abdel-Latif, A. Y.; Abdel-Rahim, M. A. Preparation of Quantum Size of Tin Oxide: Structural and Physical Characterization. *Prog. Nat. Sci.: Mater. Int.* **2016**, *26*, 145–151.
- (57) Liu, K.; Chen, S.; Wu, J.; Zhang, H.; Qin, M.; Lu, X.; Tu, Y.; Meng, Q.; Zhan, X. Fullerene Derivative Anchored SnO₂ for High-Performance Perovskite Solar Cells. *Energy Environ. Sci.* **2018**, *11*, 3463–3471.
- (58) Moulder, J. F.; Stickle, W. F.; Sobal, P. E.; Bomben, K. D. *Handbook of X-ray Photoelectron Spectroscopy*; PerkinElmer Corporation, 1992.
- (59) Huang, X.; Du, J.; Guo, X.; Lin, Z.; Ma, J.; Su, J.; Feng, L.; Zhang, C.; Zhang, J.; Chang, J.; Hao, Y. Polyelectrolyte-Doped SnO₂ as a Tunable Electron Transport Layer for High-Efficiency and Stable Perovskite Solar Cells. *Sol. RRL* **2020**, *4*, 1900336.
- (60) Yang, L.; Yang, Y.; Liu, T.; Ma, X.; Lee, S. W.; Wang, Y. Oxygen Vacancies Confined in SnO₂ Nanoparticles for Glorious Photocatalytic Activities from the UV, Visible to near-Infrared Region. *New J. Chem.* **2018**, *42*, 15253–15262.
- (61) Lee, Y.; Lee, S.; Seo, G.; Paek, S.; Cho, K. T.; Huckaba, A. J.; Calizzi, M.; Choi, D.-w.; Park, J.-S.; Lee, D.; Lee, H. J.; Asiri, A. M.; Nazeeruddin, M. K. Efficient Planar Perovskite Solar Cells Using Passivated Tin Oxide as an Electron Transport Layer. *Adv. Sci.* **2018**, *5*, 1800130.
- (62) Egdell, R. G.; Rebane, J.; Walker, T. J.; Law, D. S. L. Competition between initial- and final-state effects in valence- and core-level x-ray photoemission of Sb-doped-SnO₂. *Phys. Rev. B: Condens. Matter Mater. Phys.* **1999**, *59*, 1792–1799.
- (63) Zhang, M.; Wu, F.; Chi, D.; Shi, K.; Huang, S. High-Efficiency Perovskite Solar Cells with Poly(Vinylpyrrolidone)-Doped SnO₂ as an Electron Transport Layer. *Mater. Adv.* **2020**, *1*, 617–624.
- (64) Dong, Q.; Li, J.; Shi, Y.; Chen, M.; Ono, L. K.; Zhou, K.; Zhang, C.; Qi, Y.; Zhou, Y.; Padture, N. P.; Wang, L. Improved SnO₂ Electron Transport Layers Solution-Deposited at Near Room Temperature for Rigid or Flexible Perovskite Solar Cells with High Efficiencies. *Adv. Energy Mater.* **2019**, *9*, 1900834.

□ Recommended by ACS

Rapid Microwave-Assisted Synthesis of SnO₂ Quantum Dots for Efficient Planar Perovskite Solar Cells

Zhengjie Xu, Jinwei Gao, et al.

FEBRUARY 09, 2021

ACS APPLIED ENERGY MATERIALS

READ ▶

Origins of Efficient Perovskite Solar Cells with Low-Temperature Processed SnO₂ Electron Transport Layer

Alan Jiwan Yun, Byungwoo Park, et al.

APRIL 15, 2019

ACS APPLIED ENERGY MATERIALS

READ ▶

Surface Modification of SnO₂ via MAPbI₃ Nanowires for a Highly Efficient Non-Fullerene Acceptor-Based Organic Solar Cell

Fenggui Zhao, Bin Hu, et al.

JANUARY 06, 2020

ACS APPLIED MATERIALS & INTERFACES

READ ▶

A SnS₂ Molecular Precursor for Conformal Nanostructured Coatings

Yong Zuo, Andreu Cabot, et al.

FEBRUARY 11, 2020

CHEMISTRY OF MATERIALS

READ ▶

Get More Suggestions >